David K. Fork[1]
e-mail: fork@google.com

John Fitch
e-mail: fitch@google.com

Google, Inc.,
1600 Amphitheatre Pkwy,
Mountain View, CA 94043

Shawn Ziaei
Independent Consultant
e-mail: shawn.ziaei@gmail.com

Robert I. Jetter
Independent Consultant
e-mail: bjetter@sbcglobal.net

Life Estimation of Pressurized-Air Solar-Thermal Receiver Tubes

The operational conditions of the solar-thermal receiver for a Brayton cycle engine are challenging, and lack a large body of operational data unlike steam plants. We explore the receiver's fundamental element, a pressurized tube in time varying solar flux for a series of 30 yr service missions based on hypothetical power plant designs. We developed and compared two estimation methods to predict the receiver tube lifetime based on available creep life and fatigue data for alloy 617. We show that the choice of inelastic strain model and the level of conservatism applied through design rules will vary the lifetime predictions by orders of magnitude. Based on current data and methods, a turbine inlet temperature of 1120 K is a necessary 30-yr-life-design condition for our receiver. We also showed that even though the time at operating temperature is about three times longer for fossil fuel powered (steady) operation, the damage is always lower than cyclic operation using solar power. [DOI: 10.1115/1.4007686]

Keywords: concentrating solar power, solar receiver, Brayton cycle, reliability, metal fatigue, creep, high temperature alloy, stress, strain

1 Introduction

For several decades researchers have considered using focused solar radiation to heat air in pressurized metal tubes to run Brayton cycle turbines [1–3]. The advantages include low water use; however, from a materials standpoint, tubular air receivers are challenging due to the combined effects of thermal oxidation, pressure induced stress, diurnal thermal cycling, and thermal shocks from cloud events; this paper looks at the latter three effects and explores necessary (though not sufficient) requirements.

The system diagram is illustrated in Fig. 1. A compressor and heat recovery system boosts ambient air to ~870 K and 1.0 MPa before the air enters the solar receiver. The receiver heats the air further up to ~1300 K. The heated and compressed air passes through the turbine producing shaft power and reducing the air temperature. A common drive shaft couples the turbine, compressor and electrical generator. The turbine shaft power is absorbed by the compressor and generator.

1.1 Temperature Requirement. To achieve adequate efficiency, our estimates showed that the Brayton engine's turbine inlet temperature needs to be at least 1100 K, and is preferably at or above 1300 K, and the tube temperatures are hotter than the turbine inlet because of thermal impedances. The receiver materials are therefore considerably hotter than the materials in a supercritical steam plant [4] or a pressurized water nuclear reactor; so, one needs to proceed carefully to generate design parameters. In prior work, a tubular metal air receiver demonstrated an outlet temperature of 1070 K [1]. Fuel combustion is often proposed to elevate the temperature further. Pressurized ceramic receiver tubes have also been considered to overcome the limitations of metallic tubes [5].

1.2 Lifetime Requirement. A Brayton cycle CSP plant's electrical generation is similar to utility scale photovoltaic plants because both lack storage and provide intermittent power. Therefore, the CSP hardware must compete on design life with utility scale solar photovoltaic plants whose modules have a 25-yr warranty. We also considered replacing the receiver at intervals less than 30 yr. The cost of high temperature, oxidation resistant superalloys that can operate at or above 1070 K exceeds the cost of mild steel by at least 25×. Our cost estimates for the receiver (which are beyond the scope of this paper) suggest that the receiver needs a design life of 30 yr while operating 10 h per day.

1.3 Safety Considerations. U.S. jurisdictions normally require compliance with ASME Boiler and Pressure code for permitting. However, except for nuclear class components, no other ASME section offers guidelines for fatigue life calculation. Some other international jurisdictions also use the ASME code but even if they do not, the cyclic life evaluation procedures are generally analogous to Section III, Subsection NH [6] (hereafter referred to as Subsection NH), i.e., the French elevated temperature nuclear code RCC-MR. The life estimation methods as demonstrated in Subsection NH were specifically designed for nuclear class components, where accidents can have devastating results. Failure of a Brayton cycle receiver on the other hand results in a mild pressurized-air leak. The relative hazards are not comparable; hence, less conservatism may be justified and lifetime considerations relate mainly to tolerable repair or replacement intervals.

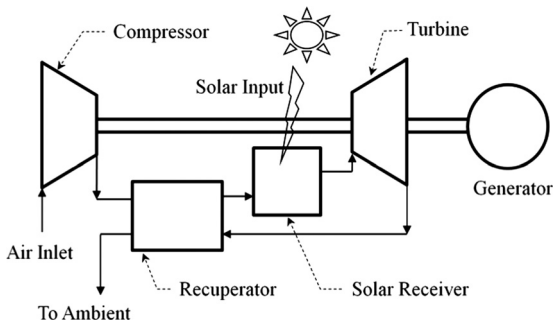

Fig. 1 Simplified schematic of a Brayton cycle solar-thermal power plant

[1]Corresponding author.

Contributed by the Solar Energy Division of ASME for publication in the JOURNAL OF SOLAR ENERGY ENGINEERING. Manuscript received February 27, 2012; final manuscript received September 19, 2012; published online October 19, 2012. Assoc. Editor: Wojciech Lipinski.

1.4 Cycling Loads. While base load power plants operate for months under steady loads, peaker plants such as combined cycle plants are often operated several hours a day based on utilities' demand. These plants are designed for infrequent cold startups; daily "hot or warm" startups have smaller load amplitude compared to a cold start. In comparison, a solar-thermal receiver experiences daily cold startup with frequent warm startup/shutdown cycles during every cloud passage.

Heat transfer through the tube wall induces a temperature gradient when the solar flux is present. Whereas some thermal stresses, such as *cross-tube* thermal gradients can be partially relieved by carefully designed strain relief structures, *cross-wall* thermal gradients are necessary for heat transfer and are hence unavoidable; we consider the latter only in this study. It is also worth noting that in real practice, heat exchangers often fail at the joints, a reliability topic not addressed here.

The tube is illustrated in Fig. 2. Heat flux Q (W/m^2) through the tube is azimuthally uniform; this is justified for well-spaced receiver tubes placed before a high reflectance insulator [7]. The cross-wall temperature gradient is given by

$$T_{\text{out}} - T_{\text{in}} = \frac{Q\phi_{\text{out}}\ln(\phi_{\text{out}}/\phi_{\text{in}})}{2k}, \tag{1}$$

where ϕ (meters) represents tube diameter, T (K), temperature, and k (W/m K) the tube alloy's thermal conductivity. Design optimization of pressurized-air heat transfer [7] resulted in a peak heat flux (including solar flux and reradiation within the receiver) of about 170 kW/m^2 on the tube. This produces a thermal gradient of about 7000 K/m in the high temperature alloys suited to the application. Absent stress relaxation, the temperature gradient in the tube wall causes the outside to expand more than the inside which places the outside under compression and the inside under tension. This balanced stress gradient is biaxial in the z (axial) and θ (tangent) directions. The maximum thermal gradient stress values occur at the surfaces and are expressed as

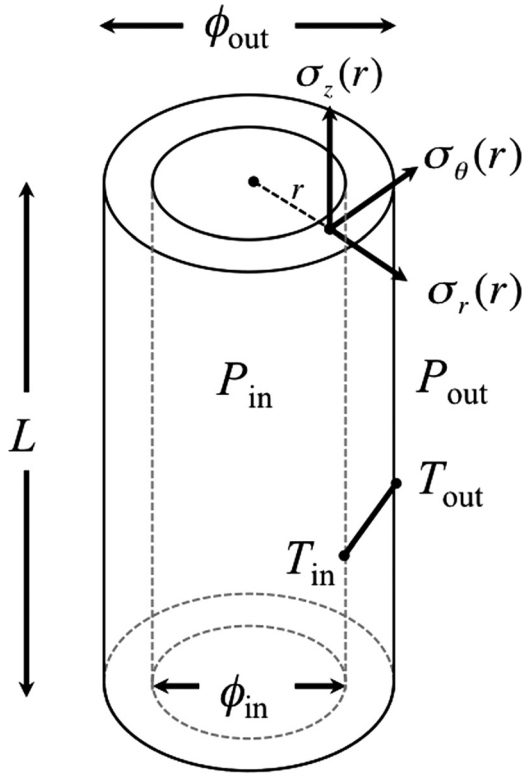

Fig. 2 Tube section schematic illustrating cross-wall thermal gradient

$$\sigma_{\text{th,max},z} = \sigma_{\text{th,max},\theta} = \frac{E}{2(1-\nu)}\alpha(T_{\text{out}} - T_{\text{in}}) \tag{2}$$

where E, ν, and α are the Young's modulus (Pa), Poisson ratio, and thermal expansivity (1/K), respectively. The thermal load in the expression above is a maximum because at elevated temperature, the material can relax via inelastic deformations. Equation (2) predicts that the stress levels can be considerably higher than the pressure induced load, σ_{P}

$$\sigma_{\text{P,z}} = \frac{P_{\text{in}}\phi_{\text{in}} - P_{\text{out}}\phi_{\text{out}}}{\phi_{\text{out}} - \phi_{\text{in}}} \tag{3}$$

$$\sigma_{\text{P},\theta} = \sigma_{\text{P,z}} + \frac{\phi_{\text{in}}^2\phi_{\text{out}}^2(P_{\text{in}} - P_{\text{out}})}{r^2(\phi_{\text{out}}^2 - \phi_{\text{in}}^2)} \tag{4}$$

$$\sigma_{\text{P},r} = \sigma_{\text{P,z}} + \frac{\phi_{\text{in}}^2\phi_{\text{out}}^2(P_{\text{in}} - P_{\text{out}})}{r^2(\phi_{\text{out}}^2 - \phi_{\text{in}}^2)} \tag{5}$$

where P is the fluid pressure. Pressure loads, unlike thermal loads cannot relax away by inelastic mechanisms.

2 Receiver Architecture and Thermal Profile

Our look-down receiver is illustrated in Fig. 3 and stems from a 3 MW-thermal design study [7]. We simulated the sun's path, heliostat field, and receiver geometry, to map the heat flux distribution in the receiver cavity. The receiver tubes are arrayed cylindrically, with compressed air flowing from bottom to top. A reflective wall of refractory insulation resides just behind the tube array. Sunlight enters through the cavity aperture and is either absorbed or reflected on a tube or reflective wall. Ray tracing software predicted a flux distribution on all receiver surfaces. Substantial spacing between the tubes allowed sunlight to bounce off the refractory wall and on to the "shaded" rear face of the tubes.

We want to assess reliability at the hottest and most heavily stressed points that fail fastest; hence, we can simulate a small section. Figure 4 shows the steady state temperature of the ID and the OD as a function of distance along a tube of 5 mm thickness

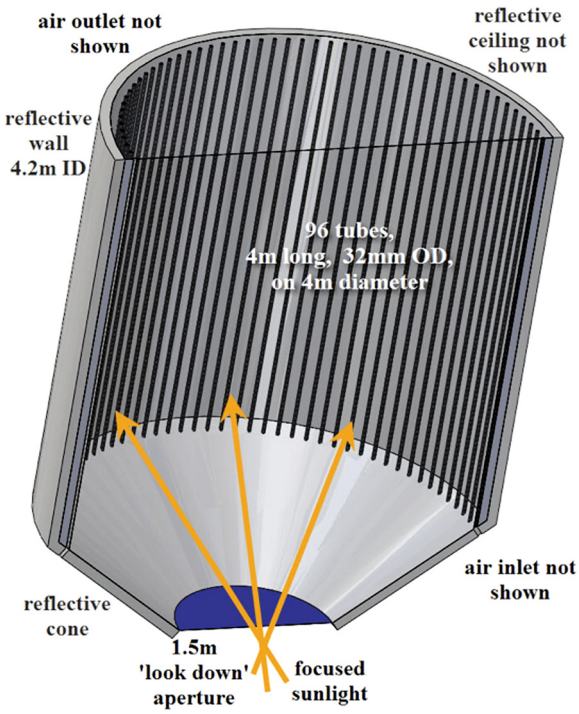

Fig. 3 Look-down receiver architecture

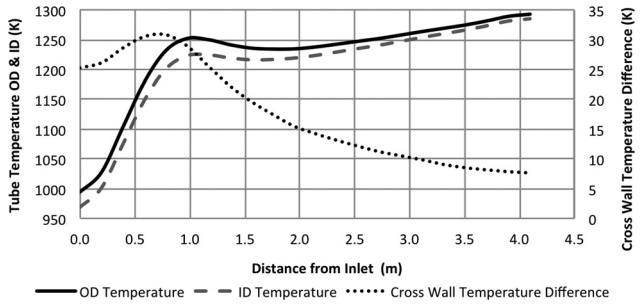

Fig. 4 Tube temperatures versus distance

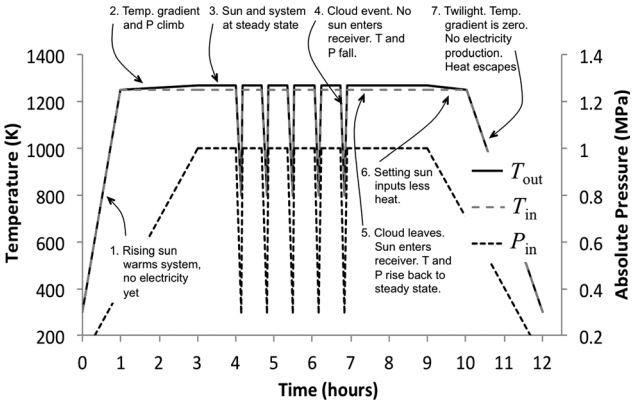

Fig. 5 Temperature and pressure time series for the daylight portion of a diurnal cycle, including five cloud events

from inlet to outlet. The tube section with the largest cross-wall temperature gradient (31 K) is approximately 0.7 m from the inlet. The highest gradient location is not the highest temperature location; both locations require consideration.

For transients, the temperature gradient was scaled back using Fourier's law through the tube wall, combined with a system model. Thermal inertia in the receiver's metal mass was included. This allowed us to predict temperature and pressure at the maximum flux location, versus time. We assumed that the outer pressure remains at an ambient value of 0.1 MPa-absolute or 0 MPa-gauge. The internal pressure was ramped to a maximum of 0.9 MPa-gauge for all cases based on a system model employing a turbine design specifically for a CSP plant [7]. The operating pressure was chosen based on a multivariable optimization of levelized cost of electricity that factored in both hardware costs and operating efficiency. For sunny days, the inner and outer temperatures rise in the morning, hold at a steady value for 6 h, and fall in the evening.

The duration and coverage of cloud events vary considerably. We modeled a slow moving cloud front by simulating an 8-min interruption of the solar flux. We used a simulation of the transient response of the receiver and engine during the solar flux interruption to define a time history of the temperature and pressure of the receiver tube.

Figure 5 shows the predicted temperatures and pressure in the tubes for a model cloudy day, with start up plateauing to steady state, five cloud events, and an afternoon ramp down. Sunlight is shaved from the peak of the day, making the system more constant. The cloud events block the sunlight for 8 min; but, thermal inertia and reradiation inside the cavity, allows the engine to operate at a reduced rate. To simplify the temperature and pressure parameters prescribed in the ANSYS mechanical model, the temperature and pressure changes were prescribed as piecewise linear. This is a very reasonable approximation of our thermal model results.

We also ran simulations of steady operation conditions under which the receiver tube is heated and pressurized instantaneously to the peak temperature conditions, and then maintained at those conditions for at least 90 days. This was done to compare the effects of diurnal cycling to a baseload power scenario.

We studied four combinations of temperature and tube-wall thickness (Table 1). The temperature range from 1100 K to 1250 K spans conditions from low-metallurgy risk and poor turbine-cycle efficiency to the edge of the code case for alloy 617 wherein thermal-to-mechanical conversion efficiency is close to 30%. At each temperature, 1100 K, 1175 K, and 1250 K, we ran one case using imperial tube gauges that exceeded the minimum tube thickness, d_{min} from the ASME Section VIII, Div 1, UG-27(c)(1) design rule

$$d_{min} = \frac{P_{in}\phi_{in}}{2(\sigma_{allowed} - 0.6P_{in})}, \quad (6)$$

where $\sigma_{allowed}$ is the allowable design stress based on the ASME Boiler and Pressure Vessel Code Section II Part D. For alloy 617, $\sigma_{allowed}$ is plotted in Fig. 6. To explore reducing thickness to reduce the thermomechanical loading, at 1250 K we also included a simulation with the thickness set to d_{min}. The simulation conditions are summarized in Table 1. Table 1 also shows the maximum thermal stress calculated from Eq. (2) based on a temperature gradient of 7000 K/m; thinner walls have smaller thermal stresses illustrating the thickness tradeoff between hoop strength and thermal loading.

3 Receiver Tube Material Properties

Temperature dependent modulus, yield strength, thermal expansivity, and thermal conductivity data are readily available for alloy 617. More challenging is the model of inelastic strain rate $\dot{\varepsilon}_i(\sigma, T)$ (1/s). Most simulations assume time-independent strain rate models; however, real materials exhibit higher (primary) creep rates initially before the steady state (secondary creep). Stress relaxation measurements (constant total strain) exhibit much higher strain rates for an applied load than creep elongation (constant load) measurements. Baseload power plants spend long periods (weeks) under steady conditions during which secondary creep is an accurate description. In a solar-thermal plant, frequent thermal shocks impose larger loads than the pressure loads. Therefore we compare models based on both equilibrium creep and stress relaxation measurements. Ideally, one would employ a unified viscoplastic constitutive model in a code such as ANSYS or ABAQUS; such development is underway [8] and will be of interest when available.

After simulation, damage estimation requires material specific creep and fatigue failure data. Creep failure estimation requires time-to-rupture, $t_{allowed}$ as a function of load and temperature. Fatigue damage estimation relies on cycles to failure N_f as a function of the strain range and temperature. Material variation causes data

Table 1 Tube geometries and peak thermal loads for simulated peak operating temperatures

Peak ID temperature (K)	Stress allowed (MPa)	Inside diameter (mm)	Minimum thickness, d_{min} (mm)	Simulation thickness(es) (mm)	Maximum thermal stress(es) (MPa)
1100	24	29.3	0.6	1.24	19.5
1175	12.2	22.1	0.9	1.65	24.8
1250	5.5	19.9	1.8	1.8, 2.77	25.8, 39.7

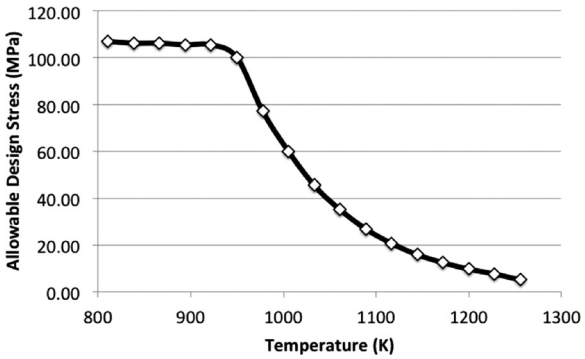

Fig. 6 Stress allowed for alloy 617

Table 2 Creep model parameters for alloy 617

Parameter	Symbol	Value	Units
A_{creep}	Creep rate coefficient	3.4×10^{31}	s^{-1}
m	Creep exponent	5.34	
U_{creep}	Activation energy	450	kJ/mol

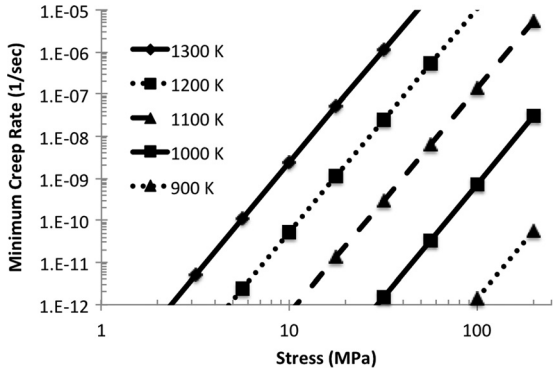

Fig. 7 Minimum creep rate correlation for alloy 617

scatter; hence, it is we note the use of *average* versus *minimum* values for creep and fatigue strength.

3.1 Alloy 617 Material Properties. We considered alloy 617 (UNS N06617), a solution strengthened alloy of nickel, chromium, cobalt and molybdenum. Basic physical property data for alloy 617 are available on the manufacturer's web site [9]. Alloy 617 is covered by the ASME Code for loads up to 1255 K (Fig. 6).

Both relaxation and secondary creep rate of alloy 617 has been characterized recently by Wright [10]. Relaxation characterizes stress decay via creep and/or plasticity at constant total strain. Equilibrium creep characterizes the steady state strain rate under constant load. Wright provided an equilibrium creep correlation based on the expression

$$\dot{\varepsilon}_i = -A_{creep}\left|\frac{\sigma_{vM}}{E(T)}\right|^m \exp\left(-\frac{U_{creep}}{RT}\right) \tag{7}$$

where the parameters are given in Table 2. Figure 7 shows a plot of the creep rate over the range of relevant stresses and temperatures based on this fit.

The relaxation rate of alloy 617 has also been characterized at 800 °C and 950 °C recently by Wright [10]. We generated a preliminary correlation to the relaxation data of Wright in the same functional form as the creep correlation where the parameters are given in Table 3.

Table 3 Relaxation model parameters for alloy 617

Parameter	Symbol	Value	Units
A_{relax}	Relaxation rate coefficient	1.15×10^{26}	s^{-1}
m	Relaxation exponent	3.3	
U_{relax}	Activation energy	450	kJ/mol

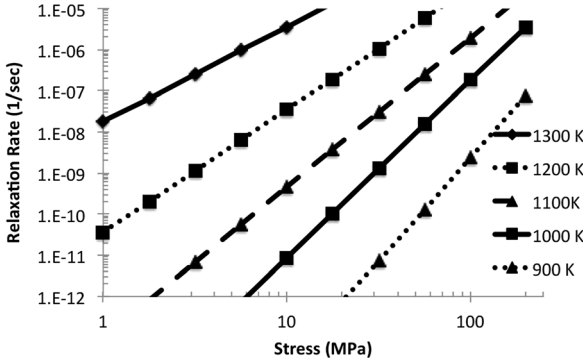

Fig. 8 Strain relaxation rate correlation for alloy 617

Figure 8 shows a plot of the relaxation rate over the range of relevant stresses and temperatures based on this fit. To check this correlation, we ran simulations of continuous fatigue and creep-fatigue cycle experiments on alloy 617 at 1223 K. Wright reported fifteen experiments over total-strain ranges of 0.3–0.6% and hold times of 0–30 min [11]. The relaxation model predicted the inelastic strain range of the cycles to within about 3% after accounting for experimental uncertainty whereas the creep model underestimated the inelastic strain by on average about 19%. Wright's smallest experimental strain ranges are still nearly 10× larger than what we simulate, so validation for the relaxation model is preliminary.

The relaxation rates (Fig. 8) are higher than the creep rates (Fig. 7) particularly at high temperature and low stress. At the load and temperature conditions, we expect the receiver to see, the relaxation and creep correlations for 617 can differ by over 4 orders of magnitude. Neither correlation is appropriate for all receiver operating conditions; however, the two strain rate correlations bracket the range of expected behavior from short to long time scales.

3.2 Creep Rupture Time for Alloy 617. The creep rupture time, $t_{allowed}$, for alloy 617 has recently been fit using the Mendelson–Roberts–Manson (M–R–M) correlation by Eno et al. [12] who published the following expression based on average creep rupture data

$$\log_{10}(t_{allowed,avg}) = -20.07 + 37531\left(\frac{1}{T}\right) + 1.20\log_{10}(\sigma) - 7568\log_{10}(\sigma)\left(\frac{1}{T}\right) \tag{8}$$

where $t_{allowed}$ is in hours, σ is in MPa, and T is in K. Eno et al. also considered the uncertainty in model parameters and produced a similar expression to describe minimum values for creep rupture time. For example, the minimum $t_{allowed}$ for the 95th percentile of the standard normal distribution is given by the following expression:

$$\log_{10}(t_{allowed,min}) = -20.66 + 37531\left(\frac{1}{T}\right) + 1.20\log_{10}(\sigma) - 7568\log_{10}(\sigma)\left(\frac{1}{T}\right) \tag{9}$$

Table 4 Fatigue correlation parameters for alloy 617

Temperature (K)	C_e	β_e
811–977	0.0137	−0.12
977–1144	0.0066	−0.09
1144–1255	0.0047	−0.08

which predicts that $t_{allowed}$ is about 3.9 times ($10^{0.59}$) shorter than for the average case. This illustrates the fairly large uncertainty depending upon whether one is designing to the material average or to the minimum.

3.3 Fatigue Failure Rate for Alloy 617. Fully reversed fatigue measurements subject a specimen through a total-strain-controlled cycle while measuring the load vs. strain hysteresis loop until the specimen fails. Yukawa [13] analyzed multiple fatigue datasets for alloy 617 in air and fit parameters to the following expression that combines Coffin-Manson (inelastic) and Basquin (elastic) terms

$$\Delta\varepsilon_{total} = \Delta\varepsilon_i + \Delta\varepsilon_e = 0.68N_f^{-0.76} + C_eN_f^{\beta e} \tag{10}$$

where $\Delta\varepsilon_{total}$ is the total-strain range, $\Delta\varepsilon_i$ and $\Delta\varepsilon_e$ are the inelastic and elastic strain ranges, respectively, N_f is the number of cycles (0.5 times the number of reversals) to failure. $C_e$and β_e are temperature dependent parameters given in Table 4.

Yukawa also published a *design* equation based on these parameters of the form

$$\Delta\varepsilon_{total} = 0.103 \cdot 0.68N_d^{-0.76} + 0.5(2/3)(1+0.3)C_eN_d^{\beta e} \tag{11}$$

which relates the total strain range, $\Delta\varepsilon_{total}$, to the allowed design cycles, N_d, by incorporating design margins into Eq. (10).

4 Finite Element Model

We simulated the receiver tube missions using ANSYS Mechanical, a general-purpose finite element tool widely used to simulate thermal and mechanical problems. Relevant for this work are the plasticity, viscoelasticity, viscoplasticity, and creep capabilities of ANSYS for simulating creep and stress relaxation at elevated temperature. As noted above, viscoplastic models for 617 would be most accurate were they available; in this work we bracketed the creep and relaxation behaviors by entering temperature dependent coefficients for Norton Law inelastic strain rate in accordance with Eq. (7). The strain rate parameters were entered in tabular form into ANSYS in approximately 30 temperature increments.

Separate simulations with each of the two inelastic strain rate models were run for each type of receiver mission. While the creep model is a better approximation to predict total inelastic strain governed by pressure induced stress, it is not able to accurately estimate stress relaxation that is dominated by thermal stress. The main requirement for this model was the capability to simulate cycling loads resulting from several months or years of operation in a timely manner. The sheer size of number of cycles (especially for cloudy days) required the model to be small and fast so that it was possible to simulate a large number of scenarios corresponding to different tube sizes, temperature ranges and tube materials.

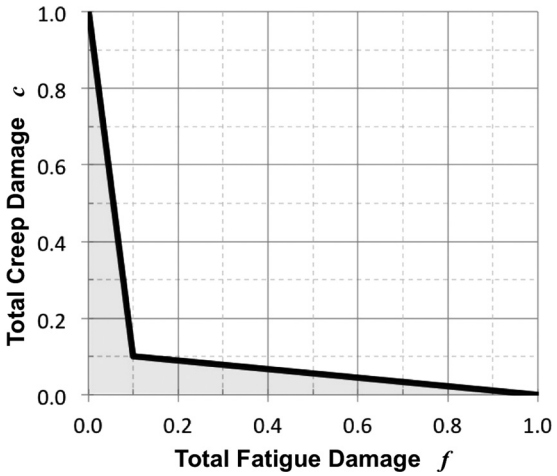

Fig. 9 Creep-fatigue interaction diagram for alloy 617

To satisfy these requirements the most appropriate element was found to be a 2nd order 2D axisymmetric structural-thermal plane element (Plane223). This eight-node element has temperature and displacement degrees of freedom and handles thermoelastic damping. The model has one axial element and 20 radial elements; the axisymmetric assumption eliminates the tangential direction.

The boundary conditions include internal pressure and axial load in addition to applied temperature at the ID and OD. The tube model was constrained axially on one end and free on the other end with the tube cross-section constrained to remain planar.

5 Life Estimation Methods

In this section, we describe two methods for estimating the mission life of the receiver tube.

5.1 Method 1: NH Life Estimation Method. This method is based on the Subsection NH of the ASME code [6,14]. The expressions below are evaluated for accumulated fatigue and creep damage.

$$f = \sum_j \frac{n_j}{N(\Delta\varepsilon_{total_j})} \tag{12}$$

$$f = \int_{t=0}^{\text{Lifetime}} \frac{dt}{t_{allowed}\left(\dfrac{\sigma_{vM}(t)}{K'}, T(t)\right)} \tag{13}$$

The quantities f and c are required to lie within the shaded region of Fig. 9. In Eq. (12), the number of allowable fatigue cycles, N, is determined from measured fatigue data based on the total (elastic plus inelastic) strain $\Delta\varepsilon_{total}$ and n_j is the number of strain cycles within the mission of type j. The equivalent strain range of a simulated load cycle, $\Delta\varepsilon_{total}$, was calculated using the method in paragraph T-1414 of Subsection NH.

$$\Delta\varepsilon_{total} = \max\left\{\frac{\sqrt{2}}{2(1+\nu)}\sqrt{\left[\Delta(\varepsilon_1-\varepsilon_2)_j\right]^2+\left[\Delta(\varepsilon_1-\varepsilon_3)_j\right]^2+\left[\Delta(\varepsilon_2-\varepsilon_3)_j\right]^2}\right\} \tag{14}$$

where each of the following time series is calculated over one diurnal cycle:

$$\Delta(\varepsilon_1 - \varepsilon_2)_j = (\varepsilon_{\text{total},z} - \varepsilon_{\text{total},\theta})_j - \max\left[(\varepsilon_{\text{total},z} - \varepsilon_{\text{total},\theta})_j\right] \quad (15)$$

$$\Delta(\varepsilon_1 - \varepsilon_3)_j = (\varepsilon_{\text{total},z} - \varepsilon_{\text{total},r})_j - \max\left[(\varepsilon_{\text{total},z} - \varepsilon_{\text{total},r})_j\right] \quad (16)$$

$$\Delta(\varepsilon_2 - \varepsilon_3)_j = (\varepsilon_{\text{total},\theta} - \varepsilon_{\text{total},r})_j - \max\left[(\varepsilon_{\text{total},\theta} - \varepsilon_{\text{total},r})_j\right] \quad (17)$$

and v, the Poisson ratio for elastic strain, is equal to 0.31.

When choosing N in Eq. (12), as noted in Sec. 5.3, the nominal N_f is less conservative than the *design* N_d. The fatigue measurements supporting this method don't include a hold-time for creep because creep is accounted for in Eq. (13). In this expression, t_{allowed} is the time to failure from creep rupture data at constant load and temperature. Subsection NH determines t_{allowed} based on the minimum strength, Eq. (9), and an equivalent stress that adjusts the von Mises stress, σ_{vM} (from simulation) by a stress safety factor, K', where $K' = 0.67$. Subsection NH does not currently cover alloy 617. $K' = 0.67$ for the alloys that Subsection NH currently does cover. Air receiver failure is not especially dangerous; hence, although not Subsection NH code-compliant, we also considered safety factor omission ($K' = 1$). The stress and temperature vary throughout the mission, so the accumulated creep damage becomes an integral over the time series that we computed from the temperature and load data from ANSYS using Simpson's rule.

Figure 9 originates from design methods developed by Corum and Blass for alloy 617 in 1989 [15] and more recently corroborated at Idaho National Laboratories [16]. Figure 9 accounts for the interaction of fatigue damage f and creep damage c, which can be significant for example when $f = 0.1$ due to the strong damage compounding that occurs when both creep and fatigue are present in appreciable amounts. Most of the data supporting the interaction diagram are for fatigue damage between 0.3 and 0.65.

As we will see, thermomechanical modeling of the solar receiver predicts low fatigue damage, so more material characterization may be warranted for application of the Subsection NH method. When we adapt Eq. (12) for our solar-thermal receiver, the fatigue term sum becomes two terms corresponding to daily total strains and cloud event strains; however, as we will see, the fatigue terms we estimate for most receiver tube scenarios explored are negligible.

5.2 Method 2: Life Estimation Based on Measured Creep-Fatigue Data. Carroll et al. [17] have measured the creep-fatigue interaction for high temperature nickel alloys, including alloy 617 and Haynes 230. These measurements include creep-hold times of up to 30 min during the fatigue strain cycle; this is analogous to the long periods of creep following diurnal or cloud driven thermal cycles. To exploit the similarity of measurement and operational conditions, we are proposing a life estimation method based on the inelastic strain amplitudes as follows:

$$F \sum_j \frac{n_j}{N_{\text{cf}}(\Delta\varepsilon_{\text{i},j})} \leq 1.0 \quad (18)$$

The design factor F is a value greater than 1, with higher values reflecting higher conservatism; $F = 20$ would be analogous with Subsection NH; however, there is no established operational basis for this. Here, we propose that $F = 10$ is prudent for a solar application given that the CSP safety considerations are minor compared to the nuclear application for which NH was developed. Given our goal of designing a receiver that will survive 30 yr we may reasonably expect that over the distribution of tubes in the receiver, some will fail at $N_{\text{cf}}/10$ cycles. N_{cf} is the creep-fatigue life determined from the inelastic strain amplitude $\Delta\varepsilon_{\text{i},j}$ of the jth type (daily cycles or cloud event types). Although it is not generally true for all high temperature alloys, for the nickel based superalloys 617 and Haynes 230, we have noted that between about 1073 K and 1200 K, inelastic strain predicts creep-fatigue life according to the Coffin Manson correlation

$$\Delta\varepsilon_{\text{i}} = C_{\text{i}} N_{\text{cf}}^{\beta_{\text{i}}} \quad (19)$$

particularly for small strain amplitudes like those in the solar-thermal receiver. As a check, we compared the predictions of correlations based on the data of Carroll et al. [17], Lu et al. [18], and more recent data [19]. At low strain amplitude the agreement between low cycle fatigue data and creep-fatigue data are close; all of the correlations that we compared agreed to within a factor of two for strain ranges smaller than 0.1%. For this study, we use the correlation published by Lu et al. in which $C_{\text{i}} = 1.39$, and $\beta_{\text{i}} = -0.8828$. We note with some caution that higher temperature data collected by Carroll et al. show that at 1273 K the fatigue damage occurs more rapidly with cycling. Therefore, for temperatures above 1200 K, one might use a temperature dependent Coffin-Manson relationship and recognize that method 2 represents a necessary but not sufficient reliability condition. If the strain cycles can be generalized to either daily strain events or cloud events, then Eq. (18) reduces to

$$10\left[\frac{n_{\text{days}}}{N_{\text{cf}}(\Delta\varepsilon_{\text{i/day}})} + \frac{n_{\text{clouds}}}{N_{\text{cf}}(\Delta\varepsilon_{\text{i/cloud}})}\right] \leq 1.0 \quad (20)$$

For missions with diurnal variation and/or clouds, the inelastic strain range, $\Delta\varepsilon_{\text{i}}$, was calculated using Eqs. (14)–(17) by substituting inelastic for total strain and by using $v = 0.5$. In Table 5, we list tube life from Eq. (12) (method 1) and Eq. (20) (method 2).

6 Results: Receiver Tube Stresses and Strains

The tube ID has higher stress at elevated temperature than the OD. Checks of creep damage integrals were higher at the ID, consistent with commonly observed internal crack initiation. Below we report only stresses and strains at the ID of the tube.

6.1 Component Stresses. To illustrate the dynamics of a diurnal cycle, Fig. 10 shows the tangential, axial and radial components at the ID of a receiver tube during two initial cloudy day cycles. Initially stress neutral, the ID assumes tensile stress as a thermal gradient develops and the OD expands more. Creep begins to relax the stress at elevated temperature during the dwell. When a cloud event occurs, removal of the gradient now results in compressive stress because relaxation has occurred. By the end of the day, relaxation is nearly complete as we see that during the night, the ID is now under compression. The tangential loads are slightly larger than the axial loads because of the additive pressure load. As expected, the radial load is minimal compared to the other components.

6.2 The Effects of Mission Type. Hereafter, we will look at the equivalent stress only. Figure 11 shows the development of equivalent stress at the ID of the receiver tube during the first 2 days of simulation using the inelastic creep model for a peak inner diameter temperature of 1250 K. The wall thickness of the tube is 2.77 mm; steady, cloudy, and sunny operation scenarios are depicted.

We see from Fig. 11 that all simulation cases approach the peak stress predicted in Table 1 during some mission portion. In the steady case, stress peaks at startup and then decays by 75% within the first 2 days. The cloudy day simulation shows the stress rise, peak, and then rise five additional times during the day due to the five cloud events. The sunny day simulation shows nearly identical stress history except for omission of the cloud event stresses. This is consistent with the brief cloud events causing negligible amounts of inelastic deformation. We also see that the nighttime

Table 5 Simulation conditions and calculated results for steady and diurnal sunny conditions

Peak ID temperature (K)	Wall thickness (mm)	Operation type	Inelastic model type	30 yr elongation (%)	30 yr creep damage: c nominal strength, no safety	30 yr creep damage: c minimum strength, $K' = 0.67$	30 yr fatigue damage: f based on Nf	30 yr fatigue damage: f based on Nd	30 yr fatigue damage: Ncf nominal	Least conservative method 1 damage	Most conservative method 1 damage	Method 2 damage
1250	1.8	Steady	Creep	0.87	0.074	2.073	—	—	—	Pass	Fail	—
1250	2.77	Steady	Creep	0.20	0.019	0.541	—	—	—	Pass	Pass	—
1175	1.65	Steady	Creep	0.17	0.006	0.205	—	—	—	Pass	Pass	—
1100	1.24	Steady	Creep	0.16	0.003	0.128	—	—	—	Pass	Pass	—
1250	1.8	Steady	Relaxation	3311.32	0.091	2.531	—	—	—	Pass	Fail	—
1250	2.77	Steady	Relaxation	1104.00	0.018	0.498	—	—	—	Pass	Pass	—
1175	1.65	Steady	Relaxation	314.01	0.005	0.167	—	—	—	Pass	Pass	—
1100	1.24	Steady	Relaxation	63.43	0.001	0.054	—	—	—	Pass	Pass	—
1250	1.8	Sunny	Creep	3.19	1.585	44.206	0.000	0.000	3.50×10^5	Fail	Fail	Pass
1250	2.77	Sunny	Creep	3.36	7.667	214.013	0.000	0.000	5.02×104	Fail	Fail	Fail
1175	1.65	Sunny	Creep	0.22	0.041	1.335	0.000	0.000	1.32×10^7	Pass	Fail	Pass
1100	1.24	Sunny	Creep	0.14	0.003	0.115	0.000	0.000	8.78×10^7	Pass	Pass	Pass
1250	1.8	Sunny	Relaxation	1170.69	0.041	1.132	0.001	4.559	3.10×10^3	Pass	Fail	Fail
1250	2.77	Sunny	Relaxation	610.38	0.037	1.042	0.000	0.395	4.56×10^3	Pass	Fail	Fail
1175	1.65	Sunny	Relaxation	171.94	0.013	0.433	0.000	0.000	1.86×10^4	Pass	Pass	Fail
1100	1.24	Sunny	Relaxation	22.98%	0.001	0.028	0.000	0.000	2.62×10^5	Pass	Pass	Pass
1250	1.8	Cloudy	Creep	2.95	1.482	41.351	0.000	0.000	3.74×10^5	Fail	Fail	Pass
1250	2.77	Cloudy	Creep	3.11	7.332	204.672	0.000	0.000	5.24×10^4	Fail	Fail	Fail
1175	1.65	Cloudy	Creep	0.20	0.038	1.245	0.000	0.000	1.41×10^7	Pass	Fail	Pass
1100	1.24	Cloudy	Creep	0.14	0.003	0.114	0.000	0.000	8.87×10^7	Pass	Pass	Pass
1250	1.8	Cloudy	Relaxation	1053.54	0.038	1.047	0.000	2.645	3.45×10^3	Pass	Fail	Fail
1250	2.77	Cloudy	Relaxation	575.33	0.037	1.036	0.000	0.276	4.77×10^3	Pass	Fail	Fail
1175	1.65	Cloudy	Relaxation	159.24	0.013	0.423	0.000	0.000	1.98×10^4	Pass	Pass	Fail
1100	1.24	Cloudy	Relaxation	20.59	0.001	0.026	0.000	0.000	2.95×10^5	Pass	Pass	Pass

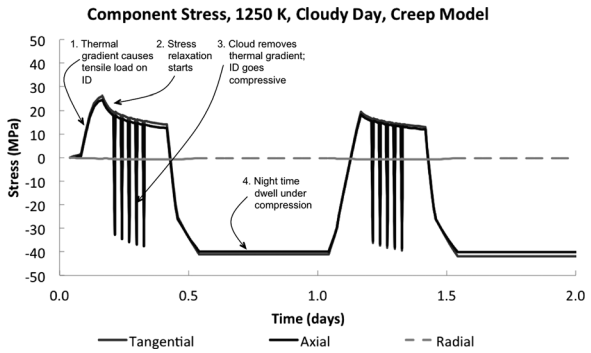

Fig. 10 Component stresses calculated using the creep model at the ID of a receiver tube during the first 2 cloudy days of operation at a peak temperature of 1250 K

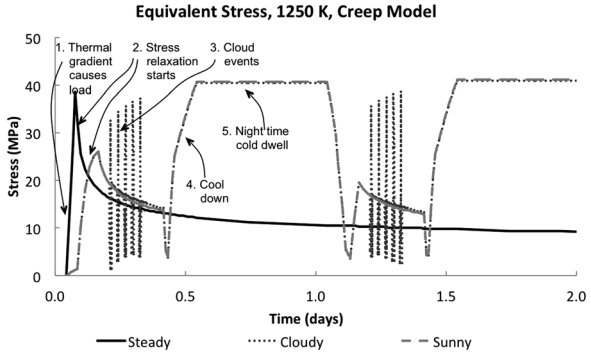

Fig. 11 Equivalent stress calculated for steady, cloudy and sunny operation during the first two days of simulation using the inelastic creep model. The peak ID temperature is 1250 K.

stress levels (second half of each day) for the cloudy and sunny days peak at the maximum thermomechanical stress predicted by Eq. (2). This is an indication that by the end of day 1, nearly all of the stress due to the thermal strain has already relaxed out, and during the high-stress, cold dwell, there is no creep damage. As the receiver tube warms the second morning, the stress falls as the thermal gradient returns; the stress reaches a minimum, and then rises further due to cool-down creep the previous day, as we will observe in Fig. 13. Stress during the hot dwell on the second sunny and cloudy days is higher at its start than at the end of the hot dwell the previous day—another illustration of creep occurring during the warm-up and cool-down phases of each day. So, whereas the relatively rapid thermal fluctuations of simulated cloud events cause an elastic response, there is a significant inelastic response from the diurnal cycle.

Figure 12 depicts the same missions as Fig. 11 at days 88–90. The tube stress in steady operation has decayed to the pressure load. The sunny and cloudy missions fluctuate to significantly higher loads. Importantly, if inelastic strain occurs during the warming and cooling cycles, the solar heat exchanger will spend much of its mission in a state of stress higher than the pressure load.

Figure 13 shows the calculated equivalent inelastic strain from the 1250 K mission for the 2.77 mm thick tube. In steady operation, the inelastic strain rises and stabilizes. The cloudy and sunny missions spend only about one-third the time at elevated temperature compared to the steady mission, but accumulate inelastic strain at a faster rate, about 3×10^{-6}/day or an elongation of 3.3% over 30 yr. As discussed earlier, these rates are a lower bound based on the creep model, which may underestimate creep rates for short perturbations. We also see from Fig. 13 that each diurnal cycle causes an inelastic strain cycle with a strain range of about 9×10^{-5}.

6.3 The Effects of Temperature and Wall Thickness. The thermal stresses can be reduced with thinner tube walls, at the cost

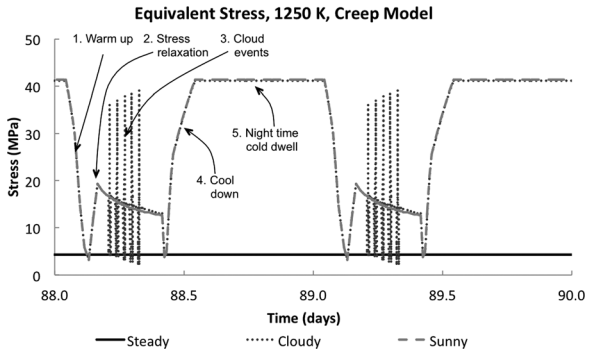

Fig. 12 Equivalent stress at the ID calculated during days 88–90 using the inelastic creep model and a peak 1250 K temperature

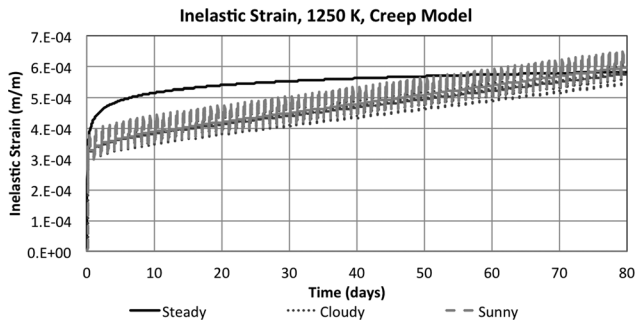

Fig. 13 Equivalent inelastic strain at the ID calculated during the first 80 days the inelastic creep model and a peak 1250 K temperature

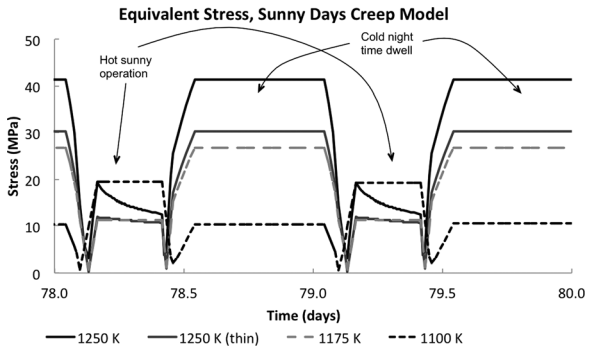

Fig. 14 Equivalent stress calculated during days 78–80 days of simulation using the inelastic creep model for the four simulations cases in Table 1

of increased pressure loads. Reduced temperature also reduces inelastic strain rates for a given load.

Figure 14 shows the time history of equivalent stress predicted during sunny days 78 and 79 using the creep model for the two thickness tubes at 1250 K, and the tubes at 1175 K and 1100 K. The thicker tube at 1250 K undergoes significant stress relaxation during the high temperature dwell, whereas the thinner tube sees smaller and steadier loads. The loads are nearly flat except during temperature ramps for the 1175 K and 1100 K missions. The high stress in the hot phase of the 1100 K mission indicates incomplete shakedown. The inelastic strain evolution using the creep model for varied wall thickness and temperature (Fig. 15) confirms that the thicker tube wall does not strengthen the receiver, because it causes an increased thermal load and larger inelastic strain range. The linear average elongation rate per day is (coincidentally)

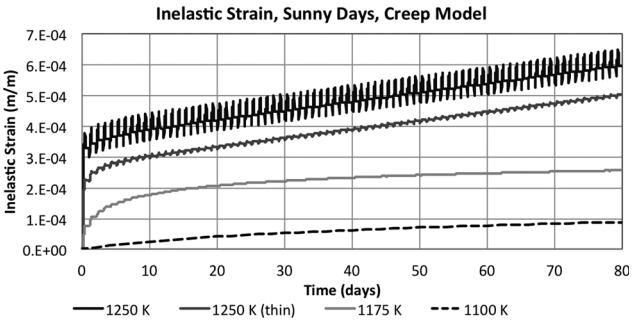

Fig. 15 Equivalent inelastic strain calculated during days 0–80 days of simulation using the inelastic creep model for the four simulation cases in Table 1

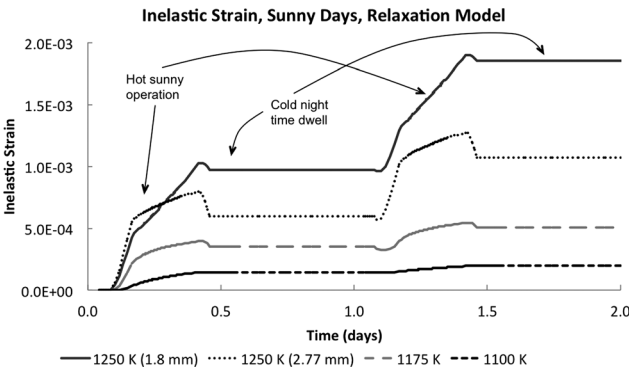

Fig. 16 Equivalent inelastic strain calculated during days 0–2 using the inelastic relaxation model for the four simulation cases in Table 1

about equal for the two thicknesses simulated at 1250 K. The inelastic strain is more asymptotic at 1175 K and 1100 K.

6.4 Relaxation Model Results. Figure 16 shows the inelastic strain that develops during the first 2 days of operation at the four mission conditions in Table 1. During hot operation, inelastic strain accumulates linearly throughout most of the day. We doubt the rapid elongation is accurate for the duration of each hot phase; but, the simulation raises the questions of (1) how fast is the initial rate of creep relaxation at the start of the day and (2) how long does it last? Relaxation is faster than equilibrium creep, but whether each diurnal cycle places the receiver tube back into relaxation mode, and how long elevated creep levels last remains unknown. The relaxation model illustrates an upper bound.

7 Results: Life Estimation

Table 5 summarizes the results of 16 simulated receiver missions. We report only sunny day operation and steady operation results; the cloudy day results were virtually identical to the sunny day results.

7.1 30 Year Elongation Results. The 30 yr elongation was calculated by fitting the linear component of the equivalent creep (see Fig. 15) at the end of each simulation and extrapolating to 30 yr. The creep model predicts realistic numbers in the range of 0–3%. We can confidently say that the relaxation model over predicts elongation for the steady case because of the large disagreement with the creep model, which is based on actual steady creep measurements.

By comparing steady and sunny day missions, we observe that diurnal cycling accelerates elongation, particularly at 1250 K where the steady elongation was 3–10 times lower even though

the hot dwell was more than 2.5 times longer. This is somewhat expected because the elongation is driven by a creep process that scales as the sum of pressure and thermal stresses raised to the fifth power; higher average loads increase elongation superlinearly.

7.2 Method 1 Damage. To estimate the 30 yr creep damage reported in Table 5, we ran the simulation to the point of stabilization, typically 90–360 days, and then integrated the creep damage in expression (Eq. (13)) for the last 7 days and then multiplied by 52×30. For the steady operation case, this represents 262,080 h of hot operation, whereas for the sunny day simulation, the receiver is hot for 109,200 h over 30 yr. As discussed above, when calculating the creep damage, there is a choice of nominal vs. minimum creep strength and whether to apply a safety factor. Table 5 reports the 30 yr creep damage integral for the two end cases: nominal creep strength with no safety factor and minimum creep strength with a safety factor of 0.67.

We calculated cycles to failure from the total equivalent strain range, $\Delta\varepsilon_{\text{total}}$. The fatigue damage portion, f, of method 1, Eq. (12), was negligible for all cases calculated with the creep model because of the small total-strain range which, according to Eq. (14), has $N_d > 10^6$ cycles. There are no cyclic loads for the steady case, so strain ranges and cycles-to-failure calculations are omitted in Table 5. Table 5 reports 30-yr fatigue damage f for both the nominal N_f (Eq. (10)) and the design N_d (Eq. (11)) cycles to failure for sunny days.

The predictions of method 1 are highly dependent on one's choices of nominal vs. minimum strength, the safety factor, and whether one uses the nominal or design cycles to failure. Some jurisdictions will require the most conservative combination. In Table 5, we report the least and most conservative combinations of these choices, using 10,920 for n_{days}.

We see that all of the steady operation cases meet the method 1 design criteria (c and f within the shaded portion of Fig. 9) with the exception of the thin (1.8 mm) tube at 1250 K for the most conservative criteria. The latter occurs because the thickness is based on Section VIII allowable stress levels and the creep damage criteria in Subsection NH are more conservative than those in Section VIII. The results are largely independent of whether the creep or relaxation model is used because for both models, the tube stresses relax to the pressure loads at long times.

We also see that for sunny (and cloudy) operation the damage estimates are highly dependent on the model choice and the level of conservatism. The creep model predicts higher stress levels and hence more creep damage. The relaxation model predicts higher strain ranges and hence more fatigue damage. Depending on one's level of conservatism, the damage estimates c and f can differ by several orders, and an additional factor of 10 or more depending on the inelastic strain model. Clearly, a narrowing of these options through better models, and a data-based set of life estimation rules is needed. Unfortunately, laboratory, or plant operation data for the combination of high temperature, low cycle amplitude, and large cycle number is not available.

What we can conclude from the range of method 1 damage calculations is that the 1250 K operating point appears risky except for steady operation; the creep model predicts failure, particularly for the thick walled tube. A viscoplastic model might predict higher life estimates if stresses relax quickly at short times and strain rates slow to secondary rates thereafter. The 1175 K operation case is marginal based on the creep damage model because it fails the most conservative strength and safety factor combination. There is a generous design space at 1100 K, and a possibility to design at higher pressure.

7.3 Method 2 Creep-Fatigue Damage Results. As with method 1, sunny and cloudy days exhibit very similar damage. Table 5 only lists results for sunny days and the failure criterion effectively reduced to $10n_{\text{days}}/N_{\text{cf}} < 1$. The strain ranges were highly dependent on whether we used the creep or relaxation inelastic strain model, the creep model being less conservative. The creep model suggests that only the thick walled tube at 1250 K would fail, and the relaxation model suggests that only the tube at 1100 K would survive. Given that the creep and relaxation models bracket the expected behavior of the inelastic strain, we expect that the actual design space lies somewhere in between the two cases. This is consistent with the life estimation results of method 1.

8 Discussion

8.1 The Pressurized-Air Brayton CSP Presents Particular Challenges. What makes air an attractive heat transfer fluid is the inexhaustible supply surrounding the power plant that obviating the need for expensive cooling and recirculation. However, air is also a poor heat transfer fluid; design considerations [7] limited the solar flux for the pressurized-air design to only 170 kW/m^2 compared to about 1000 kW/m^2 for some lower temperature, low pressure molten salt designs. In spite of the low flux, we could not predictably meet design objectives at the highest temperatures targeted. Compared to commercial CSP steam plants that operate at up to about 950 K, design for air in the 1100 K–1250 K range requires a detailed understanding of creep and much larger receiver area per unit of thermal power.

8.2 Need for Better Inelastic Models. We saw $>10\times$ predicted lifetime variation between the creep and relaxation models; but, we also expect both models capture relevant long and short-term responses to pressure and thermal loads, respectively. A general viscoplastic model [8] for the high temperature alloys of choice is needed and, when available, could narrow the range of damage predictions reported here. A viscoplastic model might predict a larger design space than we have seen. Much depends on how fast the response is to perturbations on the scale of thermal events.

8.3 Inelastic Damage Accrues Slowly. There was little difference between cloudy and sunny missions; brief thermal events like the fast passage of a small cloud bank, produced large stress responses but little creep. The most damaging thermal cycles were the diurnal cycles that occurred slowly enough for creep to occur. Although it may not be practical, this suggests that (1) a more binary application of radiation (full or none) to the receiver may have certain advantages at high temperatures and (2) more gradual cloud events than those considered here may be more damaging and may need further consideration.

8.4 Need for Better, Data-Based, Lifetime Estimates. We showed that lifetime estimates depend more than an order of magnitude on how far one relaxes conservative design rule choices based on minimum material strength and safety factors. It will take operating data or lengthy laboratory experiments under comparable conditions to establish appropriate design rules; currently, the creep rupture data are based on a load history unlike our application, and the fatigue data are based on strain rates and amplitudes unlike the receiver mission. The fatigue data we base our calculations on are isothermal; however, thermofatigue cycling can be up to $10\times$ more damaging [20] and is also time consuming to characterize.

The conventional way (method 1) of calculating fatigue damage from total strain predicts negligible fatigue, whereas method 2 based on the inelastic strain, does predict damage. It may be beneficial to avoid lifetime estimates based on summing separate creep and fatigue contributions, both of which are based on measurement conditions that differ greatly from the operational mission. Method 2 has the shortcoming that it does not address noncyclic damage. Incorporation of a second criterion, such as a total elongation limit might address this shortcoming.

8.5 The Highest Temperature Operating Condition Appears Difficult. This study casts doubt that 1250 K is a suitable design temperature for the receiver, which is somewhat disappointing because the turbine can be designed for still much higher temperature and efficiency. Thin walled tubes have lower mission damage estimates; however, especially at the highest temperatures, thin walled tubes may be susceptible to corrosion failure if the chromium can evaporate. At high temperatures diurnal cycling accelerates elongation. 1175 K may be a suitable tube ID temperature, which would result in a turbine inlet temperature of about 850 °C, not unlike past designs [1]. The design space can be more thoroughly explored; but it is prudent first to prepare better models and design criteria and to carefully examine the overall plant economics.

8.6 Steady Operation is Always Less Damaging. We see from Figs. 11 and 12 that the loads and cumulative inelastic strains are always lower for steady operation (after an initial burn-in phase). Table 5 confirms that cumulative damage is lower, even when the hot-service time is about 3 times longer. This shows that diurnal variation will make any Brayton cycle plant with a heat exchanger less reliable than baseload operation. A corollary to this is further improvements in Brayton cycle CSP plants may also make electricity from fossil energy such as coal more dispatchable, thereby increasing coal plant profitability by allowing more frequent ramping.

9 Conclusions

It is challenging to design a pressurized-air solar-thermal receiver for a Brayton cycle engine due to difficulties relating to finding adequate materials and modeling their properties. In particular, here are five key challenges:

- Time dependent creep phenomena are significant in the elevated temperature and cycle regime. Model results show that the speed and extent to which creep behaviors cycle between primary and secondary rates will have a strong influence on mechanical damage.
- The models needed to describe this creep behavior are underdeveloped.
- The data needed to produce predictive time dependent creep models are incomplete and is understandably difficult to gather because of the high temperatures and high measurement precision required for small amplitude strains.
- The extent to which conservative design parameters can be safely relaxed is not known and the sensitivity of lifetime estimates to such parameters is large: $\sim 10\times$ changes from 50% changes in safety factor for example.
- Thickness allowances for corrosion and thermomechanical fatigue effects complicate the damage assessment because lifetime estimates are highly thickness dependent.

Pressurized-air Brayton CSP plants remain an interesting concept; however, the issues raised herein must be more fully examined and resolved before costs and service life estimates can be calculated with the accuracy needed for project evaluation. Based on current data and methods, a turbine inlet temperature of 1120 K is a necessary upper limit for tube reliability in our CSP design and 1050 K is a sufficient upper limit. CSP plants require considerable cost reductions from their current status in order to compete directly with fossil energy without subsidy. Furthermore, making heat exchangers more cycle-able for use in solar applications will also increase the cycle-ability of coal powered electricity thereby making the latter cheaper and more attractive.

Acknowledgment

This paper is dedicated in memory of Timothy Allen. We acknowledge useful discussions with Kevin Chen and Ross Koningstein of Google, Philip Gleckman (now at Areva), Alec Brooks (now at AeroVironment), Darrell Socie of eFatigue, Laura Carroll, and Jill Wright of Idaho National Laboratory, Sam Sham of ORNL, Andy Jones and Gordon Tatlock of U. of Liverpool, David Metzler of Haynes Intl. and Fred Starr.

Nomenclature

A = creep rate coefficient, s^{-1}
C = fatigue coefficient
c = creep damage integral
d = tube-wall thickness, m
E = Young's modulus, Pa
F = method 2 damage factor
f = fatigue damage sum
K' = inelastic stress safety factor
k = thermal conductivity, W/m K
N = allowable cycles to failure
m = Norton creep rate exponent
n = applied cycles
P = pressure, Pa
Q = heat flux, W/m^2
R = noble gas constant, J/mol K
r = radial position, m
T = temperature, K
t = time, S
U = activation energy, J

Greek Letters

α = thermal expansivity, m/m K
β = fatigue exponent
ϕ = diameter, m
ε = strain, m/m
υ = Poisson ratio
σ = stress, Pa

Subscripts

allowed = allowance from lifetime measurement data
avg = average
cf = creep-fatigue cycles
clouds = clouds during receiver design life
/cloud = per cloud event cycle
creep = creep mechanism
days = days during receiver design life
/day = per diurnal cycle
d = design cycles
e = elastic
f = fatigue cycles
i = inelastic
in = inner, inside
j = time series subscript
max = maximum
min = minimum
out = outer, outside
P = pressure
r = radial
relaxation = relaxation mechanism
t = transients
th = thermal
total = inelastic plus elastic
vM = von Mises
z = axial
θ = tangential

Acronyms

CSP = concentrating solar power
ID = inner diameter
OD = outer diameter

References

[1] Amsbeck, L., Denk, T., Ebert, M. Gertig, C., Heller, P., Herrmann, P., Jedamski, J., John J., Pitz-Paal, R., Prosinečki, T., Rehn, J., Reinalter, W., and Uhlig, R., 2010, "Test of a Solar-Hybrid Microturbine System and Evaluation of Storage Deployment," Proceedings of SolarPaces, Pirpignan, France, September 21–24, Paper No. 0177.

[2] Stein, W., Kim, J.-S., Burton, A., McNaughton, R., Soo Too, Y. C., McGregor, J., Nakatani, H., Tagawa, M., Osada, T., Okubo, T., Kobayashi, K., 2010, "Design and Construction of a 200 kWe Tower Brayton Cycle Power Plant," Proceedings of SolarPaces, Pirpignan, France, September 21–24, Paper No. 0289.

[3] 2012, "RE<C: Brayton Project Overview," Google.org, Mountain View, CA, http://www.google.org/pdfs/google_brayton_summary.pdf

[4] Phillips, J., and Shingledecker, J., 2011, "U.S. Department of Energy and Ohio Coal Development Office Advanced Ultra-Supercritical Materials Project for Boilers and Steam Turbines, Summary of Results,"Electric Power Research Institute, Palo Alto, CA, Report No. 1022770.

[5] Smith, K. O., 1984, "Ceramic Heat Exchanger Design Methodology," Argonne National Laboratory, Argonne, Report No. ANL/FE-84-6.

[6] ASME, "2010 ASME Boiler & Pressure Vessel Code, Section III, Subsection NH, Class 1 Components in Elevated Temperature Service," The American Society of Mechanical Engineers, Fairfield, NJ.

[7] Google, 2012 "Brayton System Hardware Summary," Google.org, Mountain View, http://www.google.org/pdfs/google_brayton_system_hardware.pdf

[8] Sham, T.-L., and Walker, K. P., 2008, "Preliminary Development of a Unified Viscoplastic Constitutive Model for Alloy 617 With Special Reference to Long Term Creep Behavior," Proceedings of 4th International Topical Meeting on High Temperature Reactor Technology (HTR2008), Washington, DC, September 28–October 1, Vol. 2, Paper No. HTR2008-85215, pp. 81–89.

[9] Special Metals Corporation, 2005 "Inconel® Alloy 617," Publication Number SMC-029, http://www.specialmetals.com/documents/Inconel%20alloy%20617.pdf

[10] Wright, J. K., 2011, "Strain Rate Sensitivity of Alloy 617," Very High Temperature Reactor (VHTR) R&D 4th Annual Technical Review Meeting, Albuquerque, NM, Presentation 08 Wright J—Stress.

[11] Wright, J. K., Carroll, L. J., Cabet, C., Lillo, T. M., Benz, J. K., Simpson, J. A., Lloyd, W. R., Chapman, J. A., and Wright, R.N., 2011, "Characterization of Elevated Temperature Properties of Heat Exchanger and Steam Generator Alloys," Nucl. Eng. Des., **251**, pp. 252–260.

[12] Eno, D. R., Young, G. A., and Sham, T.-L., 2008, "A Unified View of Engineering Creep Parameters," Proceedings of ASME Pressure Vessels and Piping Division Conference (PVP2008), Chicago, July 27–31, ASME Paper No. 61129, pp. 777–792.

[13] Yukawa, S., 1991, "Elevated Temperature Fatigue Design Curves for Ni-Cr-Co-Mo Alloy 617," The 1st JSME/ASME Joint International Conference on Nuclear Engineering, Tokyo, November 4–7, pp. 1–6.

[14] Dhalla, A. K., 1991, "Recommended Practices in Elevated Temperature Design: A Compendium of Breeder Reactor Experience. (1970–1987) Volume I—Current Status and Future Directions," Bulletin 362, Welding Research Council, New York.

[15] Corum, J. M., and Blass, J. J., 1991, "Rules for Design of Alloy 617 Nuclear Components to Very High Temperatures," ASME Pressure Vessel Piping, **215**, pp. 147–153.

[16] Wright, J., and Sham, S., 2010, "Creep-Fatigue Interaction Diagram for Alloy 617 in Air at 950 °C," Engineering Calculations and Analysis Report 1199, Idaho National Laboratory, Idaho Falls, ID.

[17] Carroll, L. J., Lloyd, W. R., Simpson, J. A., and Wright, R. N., 2011, "The Influence of Dynamic Strain Aging on Fatigue and Creep-Fatigue Characterization of Nickel-Base Solid Solution Strengthened Alloys," Mater. High Temp., **27**(4), pp. 313–323.

[18] Lu, Y. L., Chen, L. J., Wang, G. Y., Benson, M. L., Liaw, P. K., Thompson, S. A., Blust, J. W., Browning, P. F., Bhattacharya, A. K., Aurrecoechea, J. M., and Klarstrom D. K., 2005, "Hold-Time Effects on Low-Cycle Fatigue Behavior of Haynes 230 Superalloy at High Temperatures," Mater. Sci. Eng.: A, **409**, pp. 282–291.

[19] Carroll, L. J., Carroll, M. C., Cabet, C., and Wright, R.N., "The Development and Impact of Microstructural Damage During High Temperature Creep-Fatigue of a Nickel-Base Austenitic Alloy," Int. J. Fatigue (accepted).

[20] Jaske, C. E., 1976, "Thermal Fatigue of Materials and Components," Report No. ASTM STP 612, pp. 170–198.